

Fully Differentiable Bidirectional Dual-Task Synergistic Learning for Semi-Supervised 3D Medical Image Segmentation

Jun Li^{a,*}

^a*School of Electrical Engineering, Southwest Jiaotong University, Chengdu, 611756, China.*

Abstract

Semi-supervised learning relaxes the need of large pixel-wise labeled datasets for image segmentation by leveraging unlabeled data. The scarcity of high-quality labeled data remains a major challenge in medical image analysis due to the high annotation costs and the need for specialized clinical expertise. Semi-supervised learning has demonstrated significant potential in addressing this bottleneck, with pseudo-labeling and consistency regularization emerging as two predominant paradigms. Dual-task collaborative learning, an emerging consistency-aware paradigm, seeks to derive supplementary supervision by establishing prediction consistency between related tasks. However, current methodologies are limited to unidirectional interaction mechanisms (typically regression-to-segmentation), as segmentation results can only be transformed into regression outputs in an offline manner, thereby failing to fully exploit the potential benefits of online bidirectional cross-task collaboration. Thus, we propose a fully **Differentiable Bidirectional Synergistic Learning** (DBiSL) framework, which seamlessly integrates and enhances four critical SSL components: supervised learning, consistency regularization, pseudo-supervised learning, and uncertainty estimation. Experiments on two benchmark datasets demonstrate our method's state-of-the-art performance. Beyond technical contributions, this work provides new insights into unified SSL framework design and establishes a new architectural foundation for dual-task-driven SSL, while offering a generic multitask learning framework applicable to broader computer vision applications. The code will be released at <https://github.com/DirkLiii/DBiSL>.

Keywords: Semi-supervised learning, Distance maps, Multi-task learning, Medical image segmentation

1. Introduction

Deep learning, predicated on data-driven paradigms, has achieved unprecedented performance across a wide spectrum of computer vision tasks. However, the empirical success of these models is critically contingent upon the scale, diversity, and annotation quality of the training data. This fundamental data dependency presents a significant bottleneck, posing substantial challenges for numerous tasks, particularly in scenarios characterized by a paucity of readily available labeled data Li et al. (2022). This issue is especially pronounced in the medical image community, where annotation demands specialized clinical expertise and physician involvement Wu et al. (2025); Li et al. (2023b). Furthermore, the typical

annotation granularity required, such as pixel-wise segmentation or slice-by-slice delineation across volumetric data, is exceedingly labor-intensive and time-consuming, frequently demanding several hours per individual sample Isensee et al. (2021). This not only imposes considerable strain on already limited healthcare resources but also significantly impedes the widespread clinical deployment and scalability of deep learning-based medical image analysis tools.

To address the challenges of data scarcity and high annotation costs, semi-supervised learning (SSL) has emerged as a compelling paradigm. It can effectively integrate both limited labeled data and readily available abundant unlabeled data into the training process, and has achieved notable success in medical image segmentation community Yang et al. (2025). Generally, most existing SSL methods are structured around two principal com-

^{*}Corresponding author.
Email address: dirk.li@outlook.com.

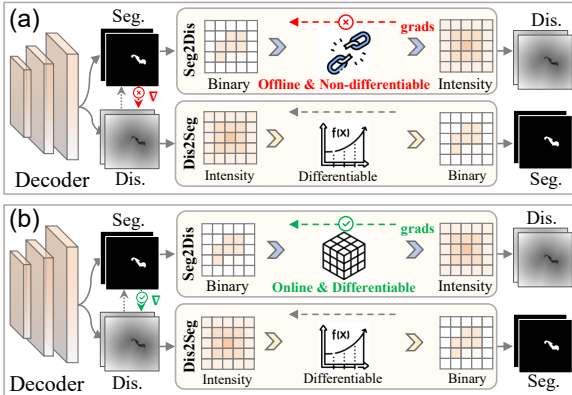


Figure 1: Different dual-task structures. (a) Unidirectional: Information flows one-way, from one task to another only. (b) Bidirectional (Proposed): Bidirectional task interaction, information can flow seamlessly between two tasks while preserving gradient continuity.

ponents: a supervised learning branch that utilizes the available labeled data, and an unsupervised learning branch that exploits the potential within the unlabeled data. The supervised component serves to establish a reliable foundation and enhance model robustness by training on ground truth labels, while the unsupervised component is designed to leverage the inherent structure, consistency, or other valuable information present in the vast pool of unlabeled data to significantly improve overall performance [Jiao et al. \(2024\)](#).

Reflecting the complexity and potential of harnessing unlabeled information, current SSL research has predominantly emphasized the refinement of the unsupervised learning component. This involves developing complex techniques to extract and discern beneficial supervisory signals from unlabeled data. Prevailing strategies include generating pseudo-labels for unlabeled samples, enforcing prediction consistency under various data augmentations or model perturbations, utilizing model uncertainty to identify reliable learning targets, or employing synergistic combinations of these techniques [Ran et al. \(2024\)](#).

Nevertheless, existing methods [Luo et al. \(2022\)](#); [Wu et al. \(2023\)](#) often underemphasize the role of labeled data within the SSL context. The learning efficacy from labeled data, however, significantly shapes model optimization trajectories. Consequently, standard supervised training alone may not fully exploit the potential of labeled data. Moreover, while there is a trend towards integrating diverse SSL techniques for richer supervision,

some approaches simply aggregate methods via parallel architectures. This may result in suboptimal information exchange, or even functional independence, between technical branches, thereby diminishing the effectiveness of the integrated strategy.

To mitigate these limitations, recent SSL studies have investigated distance regression—a task intrinsically related to segmentation, predicting the minimal distance from each pixel to the object boundary—as an auxiliary task [Luo et al. \(2021\)](#); [Li et al. \(2020\)](#). The objective is to enhance the integration of supervised and unsupervised signals through the synergistic interaction of these tasks. However, these methods often resort to offline methods to transform segmentation probability maps into distance prediction maps (Figure 1) [Ma et al. \(2020\)](#). This results in a unidirectional information flow—from regression to segmentation—hindering the establishment of a bidirectional task association. Therefore, this work aims to introduce a fully differentiable bidirectional task transformer, directly establishing gradient associations between pixel segmentation and distance regression tasks during training, thereby achieving their collaborative optimization.

To this end, we propose a **Differentiable Bidirectional Synergistic Learning (DBiSL)** framework. DBiSL employs a differentiable 3D convolution operator to emulate offline distance map generation, maintaining complete gradient flow while enabling task inter-conversion. Our core idea lies in this differentiable bidirectional transformer, designed to construct a concise yet efficient SSL system. Ultimately, DBiSL aims to synergistically enhance various SSL components, including supervised learning, consistency regularization, pseudo-labeling, and uncertainty estimation, within a global and consistent objective. Specifically, supervised learning incorporates standard segmentation supervision on labeled data, as well as cross-task supervision. The latter, facilitated by the differentiable task transformer, realizes the supervision of pixel segmentation tasks using distance regression annotations, and vice versa. Consistency regularization is predicated on the assumption that task outputs should be consistent, enforced in both pixel and distance spaces via the bidirectional transformer. Pseudo-labeling and the corresponding uncertainty estimation modules are implemented by integrating task outputs from different branches. Their primary objective is to filter high-confidence regions for pseudo-label supervision

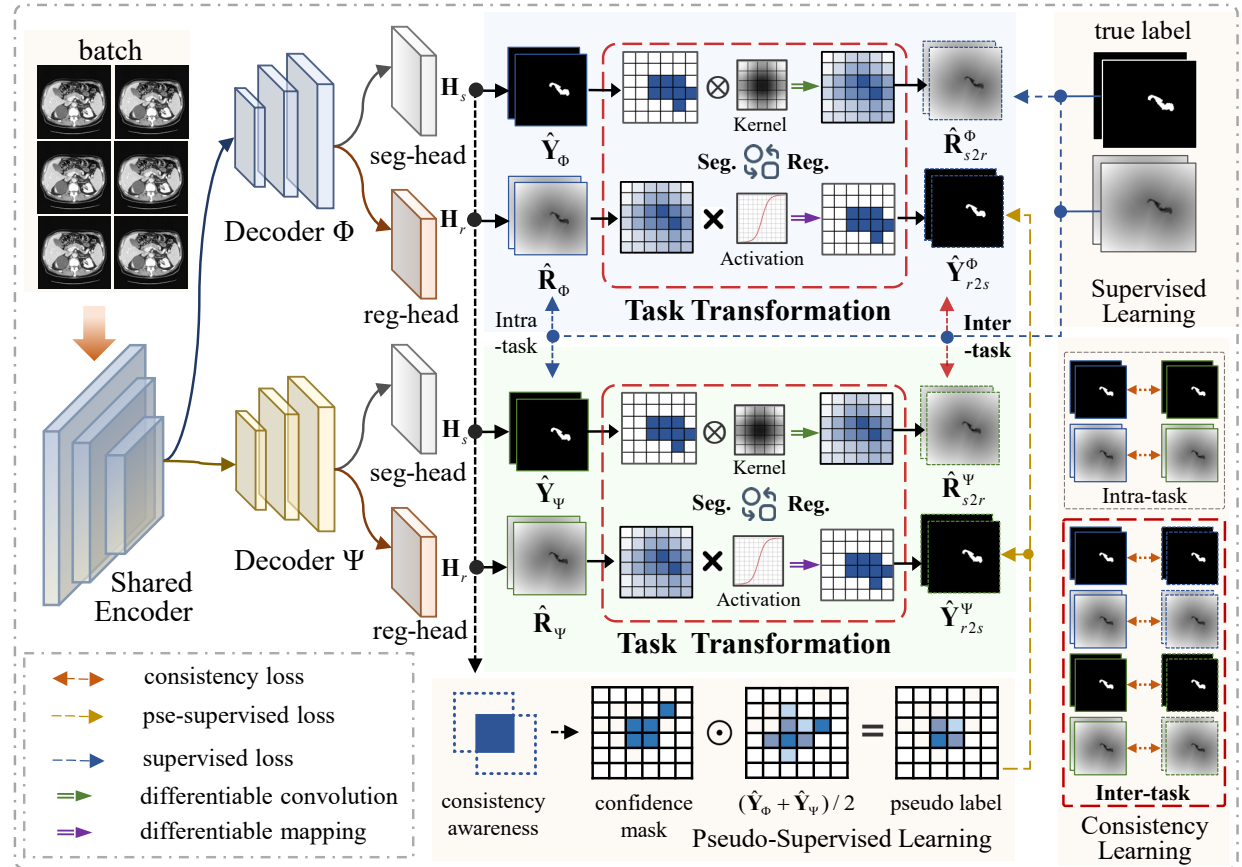


Figure 2: Overview of the DBiSL framework. A shared encoder with segmentation and distance-regression heads is coupled by our fully differentiable bidirectional task transformer, enabling online dual-task interaction and supporting cross-task supervision and cross-task consistency within a unified SSL pipeline.

and minimize noise interference.

We summarize our contributions: **(i)** a fully differentiable bidirectional task transformer, enabling gradient-propagatable inter-task interaction; **(ii)** a comprehensive SSL framework, which effectively strengthens all constraint losses through a streamlined and efficient design; **(iii)** a flexible technical architecture, offering strong compatibility with mainstream SSL techniques and notable adaptability to other vision tasks.

2. Related Work

2.1. Semi-Supervised Medical Image Segmentation

Semi-supervised learning has emerged as a promising approach to alleviate the substantial dependence of deep learning models on extensive labeled datasets, offering a promising avenue for scenarios where data annotation is costly or scarce [Han et al. \(2024\)](#). Existing methods can be broadly categorized into three categories: pseudo-labeling [Shi et al. \(2021\)](#); [Han et al. \(2022\)](#), consistency regularization [Zhu et al. \(2024\)](#); [Luo et al. \(2021\)](#); [Bai et al. \(2023\)](#); [Wang et al. \(2021\)](#), and hybrid approaches that combine elements of both [Wang et al. \(2022, 2023\)](#). Pseudo-labeling methods [Shi et al. \(2021\)](#); [Han et al. \(2022\)](#) utilize high-confidence predictions on unlabeled data as pseudo-labels, incorporating them into the training pipeline. Related researches primarily focus on developing strategies to improve the reliability and quality of the generated pseudo-labels, often employing techniques such as ensemble methods, iterative self-training pipelines, or filtering based on uncertainty. Consistency regularization approaches [Zhu et al. \(2024\)](#); [Luo et al. \(2021\)](#); [Bai et al. \(2023\)](#); [Wang et al. \(2021, 2024a\)](#), on the other hand, enhance model robustness by enforcing consistent predictions un-

der [et al. \(2024\)](#). Existing methods can be broadly categorized into three categories: pseudo-labeling [Shi et al. \(2021\)](#); [Han et al. \(2022\)](#), consistency regularization [Zhu et al. \(2024\)](#); [Luo et al. \(2021\)](#); [Bai et al. \(2023\)](#); [Wang et al. \(2021\)](#), and hybrid approaches that combine elements of both [Wang et al. \(2022, 2023\)](#). Pseudo-labeling methods [Shi et al. \(2021\)](#); [Han et al. \(2022\)](#) utilize high-confidence predictions on unlabeled data as pseudo-labels, incorporating them into the training pipeline. Related researches primarily focus on developing strategies to improve the reliability and quality of the generated pseudo-labels, often employing techniques such as ensemble methods, iterative self-training pipelines, or filtering based on uncertainty. Consistency regularization approaches [Zhu et al. \(2024\)](#); [Luo et al. \(2021\)](#); [Bai et al. \(2023\)](#); [Wang et al. \(2021, 2024a\)](#), on the other hand, enhance model robustness by enforcing consistent predictions un-

der perturbations at data, feature, network, and task levels, and may incorporate GANs [Xu et al. \(2024\)](#); [Hou et al. \(2022\)](#) or contrastive learning [Zhao et al. \(2022\)](#) for better representations. Recognizing the distinct yet complementary strengths of pseudo-labeling and consistency regularization, hybrid methods [Wang et al. \(2022, 2023\)](#) aim to synergistically integrate elements from both categories. For instance, uncertainty-aware frameworks can fuse consistency learning with uncertainty-guided pseudo-label refinement strategies [Yu et al. \(2019\)](#). While hybrid methods often yield significant performance gains, the forced integration of multiple technical pathways may introduce additional complexity to model design and the training process. Thus, this work aims to construct a concise yet efficient framework, based on our differentiable bidirectional task transformer, capable of naturally integrating the aforementioned SSL techniques without compromising training stability.

2.2. Multi-task-based Medical Image Analysis

Given that medical image analysis often necessitates performing multiple interrelated tasks on the same input data, multi-task learning has emerged as a compelling and efficient paradigm. Existing multi-task architectures developed for medical image analysis can typically be categorized into four main types based on their inter-task operational modes: cascaded [Hamghalam et al. \(2020\)](#); [Wang et al. \(2020a\)](#), parallel [Li et al. \(2023a\)](#); [Yang et al. \(2021\)](#), interactive [Zhou et al. \(2020b,a\)](#), and hybrid [Tomar et al. \(2021\)](#); [Tang et al. \(2019\)](#) architectures. Cascaded architectures process tasks in sequence, using the output of one task as input for the next, common in applications like tumor imaging with pre-training image synthesis [Hamghalam et al. \(2020\)](#). Parallel architectures, conversely, employ independent pathways for each task, typically sharing a feature encoder to enhance feature representation and segmentation accuracy, as exemplified by Aakarsh et al.’s four parallel decoders for segmentation and classification [Malhotra et al. \(2022\)](#). Interactive architectures facilitate information exchange between tasks to leverage shared knowledge; for instance, [Xu et al. \(2021\)](#) linked bladder and rectum segmentation to improve performance in complex scenarios. Hybrid architectures aim to integrate elements of the above approaches to achieve task-specific information fusion. While effective, they often rely on large-scale annotated datasets. Besides,

the potential competition between tasks may misalign optimization, prioritizing auxiliary over primary tasks. Thus, we aim to realize bidirectional task transformation and deep interaction by fostering alignment among optimization criteria, while preserving the integrity of gradient information.

3. Method

We propose a fully differentiable bidirectional task transformer and a dual-task synergistic learning framework, DBiSL, as shown in Figure 2. The framework comprises a shared encoder \mathbf{E} and two parallel decoders, $\mathbf{D}\Phi$ and $\mathbf{D}\Psi$, each equipped with segmentation and regression heads, \mathbf{H}_s and \mathbf{H}_r , to produce pixel-wise segmentation $\hat{\mathbf{Y}}$ and distance regression outputs $\hat{\mathbf{R}}$. Supervised regression labels are generated online and in a patch-based manner from segmentation labels using our task transformer, distinguishing our approach from prior work [Luo et al. \(2021\)](#); [Ma et al. \(2020\)](#); [Hu et al. \(2020\)](#); [Wang et al. \(2020b\)](#); further details are provided in Section 4. Through bidirectional task transformation and interaction, DBiSL flexibly incorporates a range of mainstream SSL techniques, yielding a hybrid model with aligned objectives. Algorithm 1 outlines the workflow. The framework leverages our proposed differentiable task transformer and incorporates popular paradigms in semi-supervised learning. It is structured around three core modules: supervised learning, consistency regularization [Luo et al. \(2021\)](#); [Bai et al. \(2023\)](#); [Wang et al. \(2021\)](#), and pseudo-supervised learning [Shi et al. \(2021\)](#); [Han et al. \(2022\)](#). We subsequently elaborate on how each component is effectively aligned with the proposed transformer, demonstrating their compatibility and synergistic integration.

3.1. Backbone Network

Although our method is model-agnostic and can be seamlessly incorporated into a broad range of segmentation backbones, we adopt the standard V-Net [Milletari et al. \(2016\)](#) architecture for fair comparisons with prior semi-supervised methods. The network comprises a single encoder and two decoders, each equipped with dropout and batch normalization. The two decoders employ distinct upsampling strategies and are attached to two task-specific prediction heads, allowing them to process the shared encoded representation independently

while jointly producing segmentation and regression outputs.

3.2. Differentiable Bidirectional Transformation

3.2.1. Regression to segmentation

There exists a strict spatial correspondence between distance maps and segmentation probability maps. The distance value for each pixel in the distance regression output can be interpreted as a measure of segmentation confidence for that pixel, specifically reflecting the degree to which the pixel's segmentation probability deviates from 0.5 [Luo et al. \(2021\)](#). When the distance regression task determines that a pixel is closer to the object boundary, the model exhibits relatively lower segmentation confidence for that pixel in the corresponding segmentation task. This is manifested as a segmentation probability that is closer to 0.5. Based on this observation, a direct conversion from regression results can be formulated as follows:

$$\hat{\mathbf{Y}}_{r2s} = \mathbf{T}_{r2s}(\hat{\mathbf{R}}) = \frac{1}{1 + e^{-k \cdot \hat{\mathbf{R}}}}. \quad (1)$$

3.2.2. Segmentation to regression

A key bottleneck in converting segmentation probability maps to distance maps lies in implementing two sequential transformations: probability maps to binary masks, and then binary masks to distance maps [Ma et al. \(2020\)](#); [Hu et al. \(2020\)](#); [Wang et al. \(2020b\)](#). While these transformations are readily performed in offline settings, the requirement for continuous gradient backpropagation within model training paradigms introduces substantial complexity. For the conversion of probability maps to binary masks, readily available built-in functions within modern machine learning frameworks offer convenient solutions. However, a definitive and differentiable solution for transforming binary masks to distance maps, especially for volumetric medical images, remains an open challenge. Inspired by [Riba et al. \(2020\)](#), we propose a fully differentiable 3D transformation method that approximates the distance transform via convolution operations, employing a custom-designed kernel \mathbf{K} to iteratively refine the precision of distance approximation:

$$\mathbf{K}(x, y, z) = \exp\left(-\frac{\sqrt{x^2 + y^2 + z^2}}{h}\right). \quad (2)$$

where (x, y, z) represents the relative spatial coordinates within the kernel, and h is a hyperparameter controlling approximation quality. To generate the signed distance map, we perform two distinct distance transform computations: one on the mask and another on its inverse ($1 - \text{mask}$), quantifying interior/exterior distances to the boundary:

$$\mathbf{S}_{in} = \mathbf{DT}(\hat{\mathbf{Y}}, \mathbf{K}), \quad \mathbf{S}_{out} = \mathbf{DT}(1 - \hat{\mathbf{Y}}, \mathbf{K}). \quad (3)$$

where \mathbf{DT} is our proposed transformer. Subsequently, these two distance maps are normalized and subtracted to yield the signed distance map [Ma et al. \(2020\)](#), which encodes both the distance to the nearest boundary and directional information:

$$\hat{\mathbf{R}}_{s2r} = \frac{\mathbf{S}_{in} - \min(\mathbf{S}_{in})}{\max(\mathbf{S}_{in}) - \min(\mathbf{S}_{in})} - \frac{\mathbf{S}_{out} - \min(\mathbf{S}_{out})}{\max(\mathbf{S}_{out}) - \min(\mathbf{S}_{out})}. \quad (4)$$

where \min and \max are the maximum and minimum functions, respectively. Thus, the transformer from the probability map to the distance map can be simply expressed as:

$$\hat{\mathbf{R}}_{s2r} = \mathbf{T}_{s2r}(\hat{\mathbf{Y}}, \mathbf{K}). \quad (5)$$

3.3. Supervised Learning

3.3.1. Intra-task supervised learning

In SSL scenarios, supervised learning is predominantly driven by limited labeled data and often relies on standard supervision strategies, potentially underutilizing rich geometric information within annotations [Jiao et al. \(2024\)](#); [Han et al. \(2024\)](#). To this end, we introduce a bidirectional cross-task supervision mechanism that leverages dense information from distance regression (pixel segmentation) labels to supervise the complementary pixel segmentation (distance regression) task. Concretely, let \mathbf{X}^l and \mathbf{Y} denote 3D medical images and segmentation annotations, the segmentation task is supervised by a weighted sum of Dice loss and cross-entropy loss, denoted as \mathcal{L}_{seg} . Thus, the normal intra-task supervision loss is:

$$\mathbf{L}_{sup}^{it} = \sum_{\omega \in \{\Phi, \Psi\}} (\mathcal{L}_{seg}(\hat{\mathbf{Y}}_\omega, \mathbf{Y}) + \mathcal{L}_{mse}(\hat{\mathbf{R}}_\omega, \mathbf{R})). \quad (6)$$

Algorithm 1 The Differentiable Bidirectional Synergistic Learning framework

Input
our model \mathbf{F}_{DBiSL} , labeled data \mathbf{X}^l , unlabeled data \mathbf{X}^u
Output
trained model \mathbf{F}_{DBiSL}
Training
for iteration $\leftarrow 0$ to max_iteration **do**
 select \mathbf{X}^l and \mathbf{X}^u from random mini-batches
 get outputs $\hat{\mathbf{Y}}_{\{\Phi, \Psi\}}$, $\hat{\mathbf{R}}_{\{\Phi, \Psi\}}$ from all heads
 get transformed outputs $\hat{\mathbf{Y}}_{r2s}$, $\hat{\mathbf{R}}_{s2r}$
Supervised learning
 build intra-task supervision \mathbf{L}_{sup}^{it}
 build inter-task supervision \mathbf{L}_{sup}^{ct}
Consistency learning
 Construct intra-task consistency \mathbf{L}_{con}^{it}
 Construct inter-task consistency \mathbf{L}_{con}^{ct}
Pseudo-supervised learning
 generate pseudo label $\bar{\mathbf{Y}}$
 generate confidence mask \mathbf{M}
 build pseudo-supervision \mathbf{L}_{pse}
 optimize model with weighted loss \mathbf{L}_{all}
return \mathbf{F}_{DBiSL}

3.3.2. Inter-task supervised learning

The distance regression labels \mathbf{R} are generated in real-time from \mathbf{Y} via our transformer \mathbf{T} . After normalization to $[-1, 1]$, negative values in \mathbf{R} pixels inside the object contour, and positive values outside. The distance regression task is supervised using the mean squared error loss \mathcal{L}_{mse} :

$$\mathbf{L}_{sup}^{ct} = \sum_{\omega \in \{\Phi, \Psi\}} (\mathcal{L}_{mse}(\mathbf{T}_{s2r}(\hat{\mathbf{Y}}_{\omega}), \mathbf{R}) + \mathcal{L}_{seg}(\mathbf{T}_{r2s}(\hat{\mathbf{R}}_{\omega}), \mathbf{Y})). \quad (7)$$

where $s2r$ ($r2s$) means the transformation from segmentation (regression) to regression (segmentation). Thus, the supervision loss can be calculated with:

$$\mathbf{L}_{sup} = \mathbf{L}_{sup}^{it} + \mathbf{L}_{sup}^{ct}. \quad (8)$$

3.4. Consistency Learning

Consistency learning has emerged as a prevalent technique within SSL paradigms Han et al. (2024); Jiao et al. (2024). The fundamental requirement

for continuous gradient propagation during training often restricts current related methods to implementing unidirectional task conversion, thereby impeding the realization of fully bidirectional inter-task interactions. We address this by leveraging our differentiable bidirectional transformer to formulate dual consistency regularization, covering both intra-task and inter-task scenarios.

3.4.1. Intra-task consistency learning

Intra-task consistency learning is based on the principle that a robust model, trained under homogeneous paradigms, should demonstrate strong agreement across its task-specific branches. In line with this, we develop an intra-task consistency mechanism to encourage greater consistency between segmentation (regression) outputs from different branches within the same task:

$$\mathbf{L}_{con}^{it} = \mathcal{L}_{mse}(\hat{\mathbf{Y}}_{\Phi}, \hat{\mathbf{Y}}_{\Psi}) + \mathcal{L}_{mse}(\hat{\mathbf{R}}_{\Phi}, \hat{\mathbf{R}}_{\Psi}). \quad (9)$$

3.4.2. Inter-task consistency learning

Cross-task consistency learning is grounded in a distinct hypothesis: an intrinsic correlation exists between pixel segmentation and distance regression tasks. Therefore, the outputs of the model for these two tasks are expected to demonstrate inherent self-consistency, rather than exhibiting mutual discrepancies. To enforce this principle, we construct an inter-task consistency loss function with transformer \mathbf{T} :

$$\mathbf{L}_{con}^{ct} = \sum_{\omega \in \{\Phi, \Psi\}} (\mathcal{L}_{mse}(\mathbf{T}_{s2r}(\hat{\mathbf{Y}}_{\omega}), \hat{\mathbf{R}}_{\omega}) + \mathcal{L}_{mse}(\mathbf{T}_{r2s}(\hat{\mathbf{R}}_{\omega}), \hat{\mathbf{Y}}_{\omega})). \quad (10)$$

Thus, the consistency learning loss is denoted as:

$$\mathbf{L}_{con} = \mathbf{L}_{con}^{it} + \mathbf{L}_{con}^{ct}. \quad (11)$$

3.5. Pseudo-supervised Learning

3.5.1. Pseudo-label generation

Effectively, the aggregation of outputs from dual-branch, dual-task architecture constitutes a simplified form of ensemble learning. This approximation effectively mitigates instabilities stemming from model initialization, distributional data biases, or intrinsic architectural constraints, thus synthesizing more robust and dependable pseudo-supervisory signals Ran et al. (2024). Therefore,

pseudo-labels $\bar{\mathbf{Y}}$ are derived by averaging the segmentation predictions:

$$\bar{\mathbf{Y}} = \frac{1}{2}(\hat{\mathbf{Y}}_\Phi + \hat{\mathbf{Y}}_\Psi). \quad (12)$$

3.5.2. Uncertainty estimation

The uncertainty estimation is performed jointly with the four results from the predictive outputs of both tasks across the dual branches. Specifically, this study employs a conservative voting strategy predicated on a "unanimous consent" principle. Under this principle, a pixel prediction is deemed reliable exclusively when the predictive outcomes from all tasks exhibit complete agreement. The construction of the confidence mask is formally represented as:

$$\mathbf{M} = \mathbb{I}(\Xi(\hat{\mathbf{Y}}_\Phi) == \Xi(\hat{\mathbf{Y}}_\Psi) == \Xi(\hat{\mathbf{R}}_\Phi) == \Xi(\hat{\mathbf{R}}_\Psi)). \quad (13)$$

where \mathbf{M} denotes the confidence mask, $==$ denotes the equality comparison, $\mathbb{I}(\cdot)$ and Ξ are the indicator function and threshold function, respectively. In summary, the pseudo-supervised learning loss can be summarized as:

$$\mathbf{L}_{pse} = \mathcal{L}_{ce}(\hat{\mathbf{Y}}_\Phi, \bar{\mathbf{Y}}) \odot \mathbf{M} + \mathcal{L}_{ce}(\hat{\mathbf{Y}}_\Psi, \bar{\mathbf{Y}}) \odot \mathbf{M}. \quad (14)$$

where \odot indicates the element-wise product. The overall loss can be summarized as:

$$\mathbf{L}_{all} = \lambda(\mathbf{L}_{sup} + \mathbf{L}_{con}) + \beta\mathbf{L}_{pse}. \quad (15)$$

where λ and β are weights that balance different losses. λ is assigned an empirical value of 0.5 and β is scheduled to increase.

4. Results

4.1. Datasets

We performed comprehensive evaluations on three public benchmark datasets: the **Left Atrium (LA)** dataset [Xiong et al. \(2021\)](#), the **Pancreas-CT** dataset [Roth et al. \(2015\)](#) and **Brain Tumor Segmentation Challenge (BraTS2019)** dataset [Menze et al. \(2014\)](#). The LA dataset consists of 100 gadolinium-enhanced 3D cardiac MRI scans, originally acquired at an isotropic resolution of $0.625 \times 0.625 \times 0.625$ mm. The Pancreas-CT dataset comprises 82 contrast-enhanced abdominal CT scans, with an in-plane resolution of 512×512 mm and slice thicknesses ranging from 1.5 to 2.5

mm. The BraTS2019 dataset comprises multi-parametric brain MRI volumes from 335 glioma subjects, where each case includes four sequences (T1, T1ce, T2, and FLAIR) and corresponding annotations for three tumor-related regions (enhancing tumor, tumor core, and whole tumor). To ensure a consistent and fair protocol, we follow the evaluation setting commonly used in prior studies [Luo et al. \(2022\)](#); [Xu et al. \(2023\)](#); [Miao et al. \(2023\)](#); [Su et al. \(2024\)](#); [Xu et al. \(2022\)](#); [Zhang et al. \(2023\)](#) and focus on WT segmentation from FLAIR, as WT delineation captures the overall disease extent and is clinically relevant for surgical planning, particularly in low-grade gliomas. We adopt the same preprocessing and split strategy as previous works: 250 volumes for training, 25 for validation, and 60 for testing. All images were uniformly resampled to an isotropic resolution of $1.0 \times 1.0 \times 1.0$ mm. Data preprocessing protocols and the stratification of labeled and unlabeled data were consistently maintained with prior studies, which is recognized as the canonical experimental setup.

4.2. Implementation Details and Evaluation Metrics

All experiments were implemented in PyTorch and executed on the NVIDIA 4080 GPU. Model training used the SGD optimizer for 17000 iterations, with an initial learning rate of 0.01 and a batch size of 4. Our model was designed to operate within a sliding window paradigm. For the LA dataset, inputs were randomly cropped sub-volumes of $112 \times 112 \times 80$ voxels, extracted with a spatial stride of $18 \times 18 \times 4$ voxels. For the Pancreas-CT and BraTS2019 dataset, a sampling window of $96 \times 96 \times 96$ voxels was utilized, with a spatial stride of $16 \times 16 \times 16$ voxels. We adopt three complementary evaluation metrics: the Dice Similarity Coefficient (DSC), the 95% Hausdorff Distance (95HD), and the Average Surface Distance (ASD). DSC quantifies the volumetric overlap via intersection over union. ASD elucidates the average surface alignment precision by computing the mean of all point-to-surface distances; 95HD focuses on capturing robust local maximum boundary deviations by considering the 95th percentile of the Hausdorff Distance. Thus, DSC evaluates global shape similarity, ASD quantifies average boundary conformity, and 95HD is sensitive to clinically relevant maximum segmentation errors.

Table 1: Comparisons with semi-supervised segmentation methods on LA dataset. Note: We only compare methods reporting results from the **final training checkpoint** (See Sec.4.3).

Method	Scans used		Metrics		
	Labeled	Unlabeled	Dice (%) \uparrow	ASD (mm) \downarrow	95HD (mm) \downarrow
Supervised baseline	16	0	82.36	3.08	11.87
Supervised baseline	80	0	91.88	1.37	4.60
TAC Chen et al. (2022)	16	64	87.75	2.04	9.45
AUSS Adiga et al. (2024)	16	64	88.60	/	7.61
MCF Wang et al. (2023)	16	64	88.71	1.90	6.32
UA-MT Yu et al. (2019)	16	64	88.88	2.26	7.32
DTC Luo et al. (2021)	16	64	89.42	2.10	7.32
SASSNet Li et al. (2020)	16	64	89.54	2.20	8.24
DUWM Wang et al. (2020c)	16	64	89.65	2.03	7.04
BaPC Wang et al. (2024b)	16	64	89.71	1.85	6.08
SCC Liu et al. (2022)	16	64	89.81	1.82	7.15
DBiSL	16	64	90.54	1.80	6.05

4.3. Evaluation Protocol and Comparison Standards

Evaluation protocols in SSL diverge into two paradigms. The first reports peak performance by selecting the optimal checkpoint based on evaluation metrics. Crucially, many existing methods achieve this by directly evaluating during training without a separate validation set. This practice introduces a significant bias, as the reported best results essentially reflect overfitting to the specific test distribution rather than true generalization. In contrast, the second paradigm evaluates performance at the final training checkpoint. To ensure a rigorous and fair assessment, our comparisons focus exclusively on methods evaluated at their final training checkpoints. We exclude methods that utilize the best iteration, as such protocols rely on information unavailable in real-world deployment and overestimate the model’s practical capability.

4.4. Comparison with State-of-the-art Methods

We conducted comparative evaluations against several state-of-the-art SSL methods in Table 1, Table 2 and Table 3, including DTC [Luo et al. \(2021\)](#), DUWM [Wang et al. \(2020c\)](#), AC-MT [Xu et al. \(2023\)](#), MCF [Wang et al. \(2023\)](#), CoraNet [Shi et al. \(2021\)](#), TAC [Chen et al. \(2022\)](#), BaPC [Wang et al. \(2024b\)](#), UG-MCL [Zhang et al. \(2023\)](#), AUSS [Adiga et al. \(2024\)](#), SCC [Liu et al. \(2022\)](#), UA-MT [Yu et al. \(2019\)](#), URPC [Luo et al. \(2022\)](#), AUA [Wu et al. \(2023\)](#), SASSNet [Li et al. \(2020\)](#),

CPCL [Xu et al. \(2022\)](#), MRPL [Su et al. \(2024\)](#) and CauSSL [Miao et al. \(2023\)](#). To minimize confounding factors from varying experimental setups across studies, we directly adopted performance metrics reported in the original publications. As shown in Table 1, DBiSL achieves the best performance on LA (90.54% Dice/1.80 ASD/6.05 95HD), consistently outperforming prior SSL baselines. On Pancreas-CT (Table 2), DBiSL attains the highest Dice score (81.09%), while remaining competitive on boundary metrics. Importantly, Table 3 further demonstrates strong generalization to brain MRI, where DBiSL achieves the best overall results on BraTS2019 (85.09% Dice/1.89 ASD/8.12 95HD). In addition, Figure 3 provides 3D visual comparisons against fully supervised and semi-supervised baselines, qualitatively confirming that our differentiable bidirectional collaboration yields more accurate and structurally consistent boundaries. Overall, these results validate the effectiveness and robustness of our synergistic learning framework enabled by the proposed fully differentiable bidirectional transformer.

4.5. Ablation Study on Key Components

To dissect the contribution of key components, we conducted the ablation study (Table 4, Figure 4), evaluating the impact of: **reg_task** (all distance regression tasks); **pse_sup** (pseudo-supervised learning); **ct_sup** (cross-task supervised learning); **all_con** (all consistency learning);

Table 2: Comparisons with semi-supervised segmentation methods on Pancreas-CT dataset. Note: We only compare methods reporting results from the **final training checkpoint** (See Sec.4.3).

Method	Scans used		Metrics		
	Labeled	Unlabeled	Dice (%) \uparrow	ASD (mm) \downarrow	95HD (mm) \downarrow
Supervised baseline	12	0	65.60	1.87	12.83
Supervised baseline	62	0	81.69	1.18	6.00
MCF Wang et al. (2023)	12	50	75.00	3.27	11.59
BaPC Wang et al. (2024b)	12	50	76.36	2.83	10.59
DTC Luo et al. (2021)	12	50	78.27	2.25	8.36
CoraNet Shi et al. (2021)	12	50	79.67	1.89	7.59
AUA Wu et al. (2023)	12	48	79.81	1.64	5.90
URPC Luo et al. (2022)	12	50	80.31	1.43	4.39
CauSSL Miao et al. (2023)	12	50	80.92	1.53	8.11
DBiSL	12	50	81.09	1.71	6.90

Table 3: Comparisons with other semi-supervised methods on BraTS2019 dataset.

Method	Scans used		Metrics		
	Labeled	Unlabeled	Dice (%) \uparrow	ASD (mm) \downarrow	95HD (mm) \downarrow
Supervised baseline	25	0	76.29	6.63	22.98
Supervised baseline	250	0	85.13	2.14	8.39
UG-MCL Zhang et al. (2023)	25	225	82.82	2.30	11.29
CPCL Xu et al. (2022)	25	225	83.36	1.99	11.74
CauSSL Miao et al. (2023)	25	225	83.54	1.98	12.53
AC-MT Xu et al. (2023)	25	225	83.77	1.93	11.37
URPC Luo et al. (2022)	25	225	84.16	2.63	11.01
MRPL Su et al. (2024)	25	225	84.29	2.55	9.57
DBiSL	25	225	85.09	1.89	8.12

ct_con (cross-task consistency); and **it_con** (intra-task consistency). Ablation results reveal that the regression task most significantly enhances performance, strongly validating multi-task learning for SSL. Pseudo-supervision and consistency regularization, as the most popular techniques, also substantially improve performance. The cross-task supervision in the supervised learning is empirically validated to effectively enhance performance. These findings clearly demonstrate DBiSL’s synergistic nature: removing any key component would degrade performance, highlighting the critical and synergistic value of modules.

4.6. Ablation Study on Unified Processing

A typical SSL approach treats labeled and unlabeled data disparately: labeled data for supervised learning, unlabeled data solely for pseudo-

supervision. The rationale is that labeled data, possessing inherent label information, seemingly negates the need for pseudo-supervision. Nevertheless, such disjointed paradigms can engender a “shortcut” effect, resulting in a processing imbalance. Thus, we tested removing labeled data from pseudo-supervision, the results in Table 5 show quantifiable performance degradation. Thus, a unified processing approach facilitates a more holistic utilization of information from all available data, mitigating biases toward specific data types.

4.7. Performance on the unlabeled training data

To evaluate pseudo-label quality, we conducted a post-hoc analysis on the unlabeled training data (Table 6). For the LA dataset, the model achieves considerable accuracy despite limited supervision, with high-confidence masks significantly improving

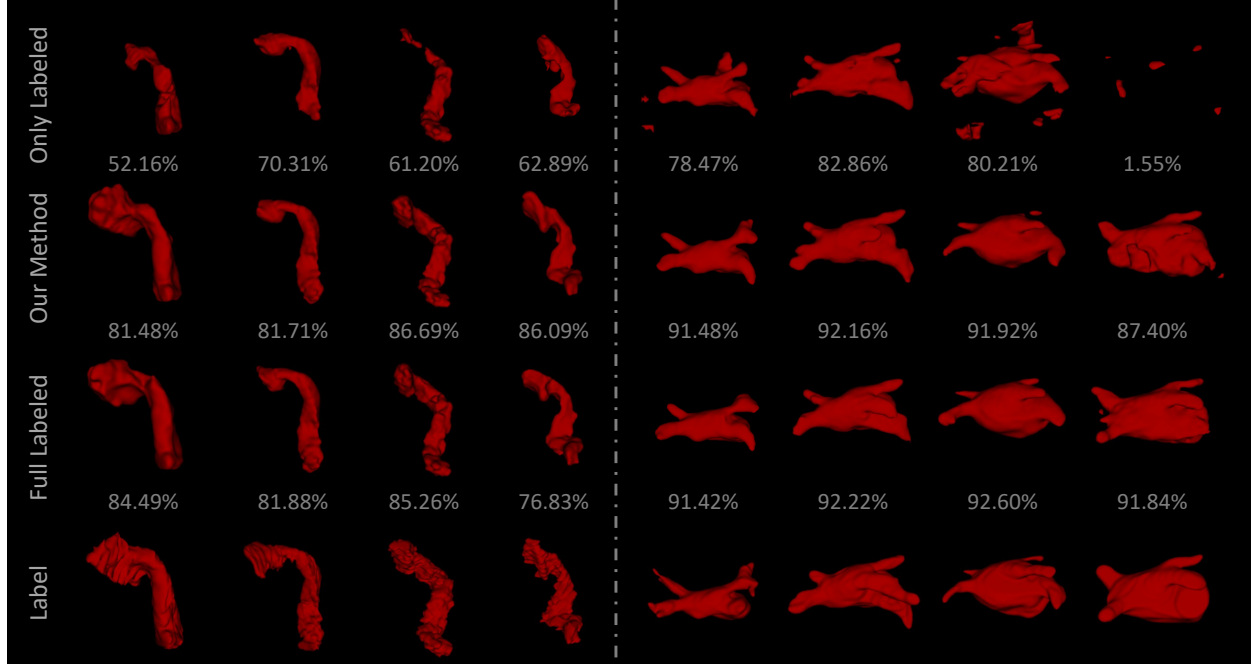


Figure 3: 3D Visual comparison of segmentation results with varying label proportions.

Table 4: Ablation study on Pancreas-CT dataset.

Method	Metrics		
	Dice (%) ↑	ASD (mm) ↓	95HD (mm) ↓
DBiSL	81.09	1.71	6.90
w/o reg_task	64.58	1.11	18.19
w/o pse_sup	66.45	4.13	13.82
w/o ct_sup	76.32	2.47	10.66
w/o all_con	68.15	1.29	20.33
w/o ct_con	71.57	1.25	14.43
w/o it_con	76.83	1.24	9.37

precision by mitigating erroneous signals. Conversely, due to the inherent segmentation challenges associated with the pancreas dataset, performance on the pancreas dataset remains inferior to the LA results, underscoring the need for specialized segmentation strategies. Consequently, future research endeavors should prioritize the exploration and integration of customized strategies specifically tailored for pancreas segmentation tasks. Overall, the model’s robust performance on unlabeled data validates the effective transition from a semi-supervised to an approximate fully-supervised paradigm.

Table 5: Ablation study on unified processing.

Method	Metrics		
	Dice (%) ↑	ASD (mm) ↓	95HD (mm) ↓
with labeled data	90.54	1.80	6.05
w/o labeled data	89.40	1.81	6.78

Table 6: Results for unlabeled training samples.

Dataset	Metrics		
	Dice (%) ↑	Recall (%) ↑	Precision (%) ↑
LA	90.11	88.60	92.26
Pancreas_CT	75.57	81.81	72.03

4.8. Performance under Various Labeling Ratios

To test the model’s stability, we evaluated DBiSL on the LA dataset using 5%, 10%, 20%, and 50% labeled data. As shown in Table 8, we compared our results against several SOTA methods. For a fair comparison, the performance metrics for these methods were taken directly from their original reports. The results show that DBiSL consistently leads other SOTA methods across all ratios. Notably, even with only 5% labels, our method

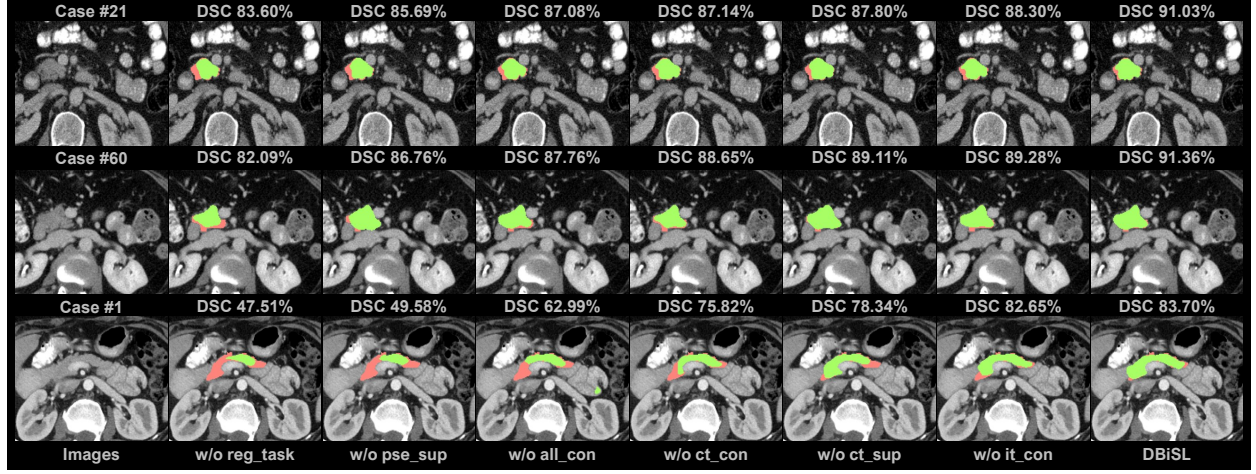


Figure 4: Visual comparison of results from the ablation study. Green and red regions delineate the outputs and the ground truth, respectively.

Table 7: Comparison of offline transformation method and our proposed online transformation method on LA dataset.

Method	DSC (%)	Time (s/case)	Diff.	GPU
offline-original	100.00	1.03	No	No
online-original	99.95	0.05	Yes	Yes
offline-resample	91.17	0.10	No	No
online-resample	97.53	0.01	Yes	Yes

achieves a Dice score of 84.62%, outperforming the baseline by a wide margin of 22.39%. This suggests that our bidirectional synergistic learning is particularly effective when labeled data is extremely scarce. While the performance gap narrows at 50% supervision, DBiSL still maintains an edge, proving its robustness across varying levels of data availability.

4.9. Precision and Computational Efficiency of Different Distance Transformation Methods

We validated our differentiable task transformer against a widely used offline method. By leveraging convolutional operations, our transformer is GPU-accelerated, offering substantial computational advantages over CPU-bound offline approaches. To alleviate computational bottlenecks, we downsample the binary mask, apply the distance transformer, and then upsample the output to the original resolution (denoted as resample in Table 7). It should be noted that our distance approximation, implemented with customized convolutional kernels, inherently introduces some precision loss.

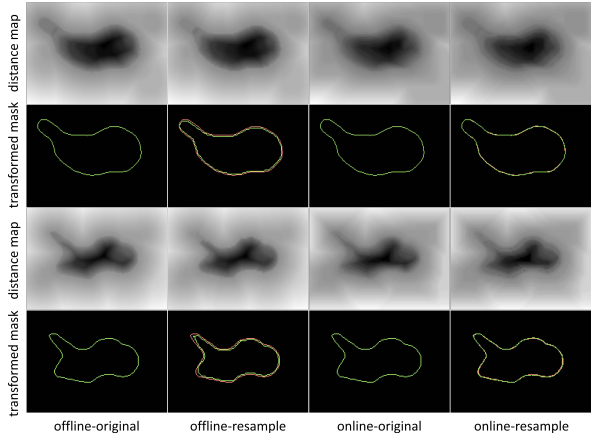


Figure 5: Visualization of different distance transform methods. Green and red contours denote transformed and label contours, respectively.

We quantified this loss by inversely transforming distance maps to segmentation masks and evaluating the DSC against ground-truth labels. As shown in Table 7 and Figure 5, the precision loss remains within acceptable margins. Moreover, because the same differentiable transformation is used in both the regression label generation and model inference, the approximation error originates from a consistent source, thereby reducing its potential adverse impact. Thus, the inherent precision loss is not expected to critically affect model performance.

4.10. Impact of Downampling Rate

Maintaining the propagation of gradient information typically incurs significant GPU memory over-

Table 8: Results with various labeling ratios.

Method	Labeling Ratios			
	5%	10%	20%	50%
Baseline	62.23	79.44	82.36	91.50
TAC	/	84.73	87.75	/
AUSS	/	86.58	88.6	/
MCF	/	/	88.71	/
UAMT	/	84.25	88.88	/
DUWM	/	85.91	89.65	/
DTC	/	87.51	89.42	/
SASSNet	/	86.81	89.27	/
BaPC	/	88.55	89.71	/
SCC	/	86.51	89.81	/
DBiSL	84.62	88.78	90.54	91.84

head. We addressed this by performing downsampling on the input prior to online distance map generation. Although we verified in the previous section that this downsampling operation has a limited impact on the intrinsic accuracy of the distance map itself, its effect on the model’s overall performance warrants further investigation. To this end, we explored different downsampling scale factors to assess the specific influence of this operation on the model’s segmentation performance. Notably, using the original full resolution for differentiable distance transform during training results in GPU memory overflow on an RTX 4080. Consequently, we set the upper bound for the downsampling scale factor to 0.5. Experimental results, presented in Table 9, are consistent with intuition: model performance is optimal when the downsampling scale factor is set to 0.5. This indicates that a lower degree of downsampling (i.e., a higher scale factor) results in less information loss introduced by the distance transform, thereby yielding higher model performance. Furthermore, it is noteworthy that the model exhibits relatively low sensitivity to this downsampling scale factor hyperparameter; the model’s overall performance remains at a high level.

4.11. The Impact of Pre-Generation and On-the-fly Generation Schemes

Existing multi-task schemes, which often integrate distance regression, are generally inefficient due to their reliance on offline distance map generation, failing to fully utilize modern GPU parallel computing power. While this pre-generation strategy is feasible for 2D segmentation (where targets are computed based on the full image regardless of

Table 9: Segmentation performance with different downsampling rate on LA dataset.

Down Rate	Metrics		
	Dice (%) ↑	ASD (mm) ↓	95HD (mm) ↓
0.5	90.54	1.80	6.05
0.3	90.40	1.59	6.69
0.1	90.01	1.58	6.83

Table 10: Performance with Pre-generated and On-the-fly Distance Maps on Pancreas-CT Dataset.

Method	Metrics		
	Dice (%) ↑	ASD (mm) ↓	95HD (mm) ↓
On-the-fly	81.09	1.71	6.90
Pre-generated	74.48	1.42	8.52

whether they are generated offline or online), it introduces a critical challenge in 3D patch-based segmentation. Due to GPU memory constraints, mainstream 3D methods use a sliding window strategy, processing only a local input patch. This leads to an inherent information asymmetry: offline targets are computed from the entire 3D volume, whereas online predictions are made solely based on the local patch information. This requires the model to infer global distance values from local context, significantly complicating the distance regression task. Our GPU-accelerated differentiable transformer provides an efficient generation paradigm that addresses this limitation. By enabling online, GPU-accelerated computation, it effectively alleviates the information asymmetry issue inherent in existing approaches (Figure 6). Comparative results (Table 10) confirm the superiority of our proposed scheme.

4.12. Computational Efficiency of Different Models

To assess the practicality of DBiSL, we report its computational footprint in Table 11 and benchmark it against strong SSL competitors. Overall, DBiSL keeps a compact architecture (12.35M parameters), comparable to MRPL and notably lighter than CauSSL (23.60M). The differentiable bidirectional coupling introduces additional computation during training, resulting in 0.492 s/iter; nevertheless, this cost remains below DTC (0.645 s/iter) and

Table 11: Computational costs of different methods on BraTS2019 dataset. G-Mem: GPU memory usage during training.

Method	Params (M)	Train (s/iter)	Test (s/case)	G-Mem (GB)
DTC	9.45	0.645	1.02	4.62
CauSSL	23.60	0.442	1.75	8.43
UA-MT	9.45	0.367	1.08	5.33
MRPL	12.35	0.334	1.67	10.40
DBiSL	12.35	0.492	1.66	9.49

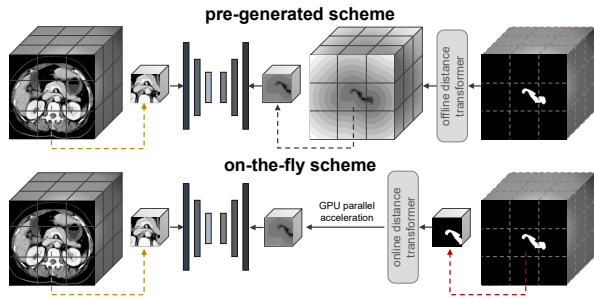


Figure 6: Workflow of pre-generated and on-the-fly schemes. The former selects corresponding patches from pre-generated full-resolution distance maps as labels for the distance regression task, while the latter generates distance labels based on the respective patches.

is within the same practical regime as other modern SSL baselines. Importantly, the proposed design does not inflate inference latency: DBiSL runs at 1.66 s/case, essentially matching MRPL (1.67 s/case) and slightly improving over CauSSL (1.75 s/case). Regarding memory, DBiSL requires 9.49 GB during training—higher than lightweight consistency baselines such as UA-MT (5.33 GB), yet lower than MRPL (10.40 GB)—and thus remains compatible with commonly available GPUs for 3D segmentation. These results suggest that the additional differentiability-enabled collaboration yields improved accuracy while preserving a practically deployable computational profile.

4.13. Backbone Generality.

We further instantiate DBiSL with nnU-Net [Isensee et al. \(2021\)](#), DiffUNet [Xing et al. \(2025\)](#), and SegMamba [Xing et al. \(2026\)](#) on the LA dataset under the same labeled/unlabeled split. As shown in Table 12, replacing V-Net with nnU-Net or DiffUNet yields comparable Dice scores (90.09%/90.13% vs. 90.54%), supporting the plug-and-play nature of our SSL paradigm. We note that, due to GPU memory constraints, we reduce

Table 12: Performance with four backbones on LA dataset.

Backbone	DSC (%)	ASD (mm)	95HD (mm)	Params (M)
V-Net	90.54	1.80	6.05	12.35
nnU-Net	90.09	2.45	11.69	48.36
DiffUNet	90.13	2.63	11.56	80.18
SegMamba	88.88	3.15	11.61	86.87

We reduce the patch size to $64 \times 64 \times 64$ for SegMamba and $96 \times 96 \times 96$ for nnU-Net and DiffUNet to avoid overflow.

the patch size to $96 \times 96 \times 96$ for nnU-Net and DiffUNet and to $64 \times 64 \times 64$ for SegMamba; the smaller 3D context may weaken global anatomical continuity modeling and thus negatively impact boundary-sensitive metrics, which likely contributes to the relatively lower performance of SegMamba in our current setting. Overall, these results indicate that the gains of DBiSL are not specific to a particular network design, but stem from the proposed learning scheme. At the same time, they suggest that extracting the best performance from large-capacity backbones in extremely low-label settings can be sensitive to resource-dependent choices (e.g., patch size) and backbone-specific training recipes.

5. Discussion

5.1. Difference from Unidirectional Segmentation-regression Synergistic Methods

This work is closely related to DTC [Luo et al. \(2021\)](#) in that both exploit the complementarity between segmentation and distance regression under SSL and are evaluated on overlapping benchmarks. However, DTC essentially yields a unidirectional synergy, where the auxiliary regression branch mainly provides guidance to improve segmentation. Such one-way interaction prevents segmentation-derived structural cues (e.g., explicit boundary/topology information) from being fed back to refine distance regression during training, thereby limiting mutual task reinforcement. In contrast, we introduce a fully differentiable bidirectional task transformer that enables end-to-end, reciprocal information exchange between the two tasks (regression \rightarrow segmentation and segmentation \rightarrow regression). Targeted ablations (Table 13) further verify the necessity of bidirectionality: DBiSL achieves 81.09% DSC with 6.90 mm 95HD, while the fully differentiable unidirectional variants drop

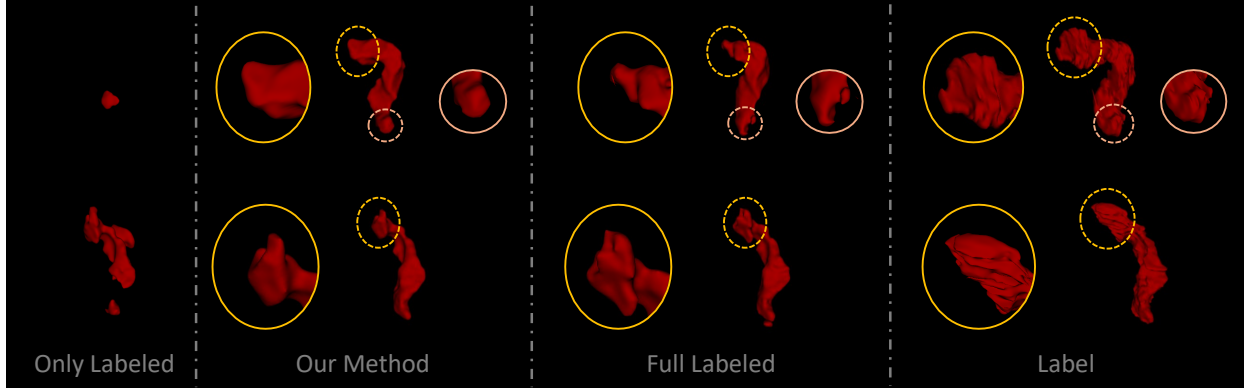


Figure 7: 3D visualization of two cases demonstrating poor segmentation performance.

Table 13: Performance of unidirectional and bidirectional synergistic methods.

Method	Metrics		
	Dice (%) ↑	ASD (mm) ↓	95HD (mm) ↓
DBiSL	81.09	1.71	6.90
DBiSL-S2R	68.79	1.16	17.65
DBiSL-R2S	71.59	1.12	16.77

markedly to 68.79%/17.65 mm (DBiSL-S2R) and 71.59%/16.77 mm (DBiSL-R2S), indicating that one-way guidance is insufficient to resolve the mutual dependency and latent conflicts between the two tasks under scarce supervision.

5.2. Difference from Other Multi-task Learning Methods

This work is distinguished from existing dual-task driven methods in three key aspects. First, for the synergy mechanism, our DBiSL achieves bidirectional information interaction, as elaborated in Sec.5.1. Second, for the framework construction, DBiSL presents a comprehensive and self-consistent framework. It integrates essential SSL components—pseudo-supervision, confidence estimation, consistency regularization, and supervised learning—overcoming limitations of isolated techniques by unifying them under a coherent objective. Third, for the training paradigms, we leverage GPU parallelism for real-time patch-based distance map generation within each mini-batch. This contrasts with offline pre-computation in prior methods, which, while reducing CPU load in training, forces models to infer global context from local patch—potentially hindering training.

5.3. Analysis of Failure Cases

Figure 7 illustrates the segmentation results of our proposed method, the baseline (Only Labeled), and the theoretical upper bound (Full Labeled) on two challenging samples. As observed, both our method and the Full Labeled approach achieve relatively accurate segmentation of the pancreatic body. However, their segmentation performance significantly degrades when it comes to the head and tail regions of the pancreas. This phenomenon is primarily attributed to the high variability of the pancreatic anatomical structure and its indistinct boundaries with surrounding tissues Li et al. (2025). Specifically, the pancreatic body, being the central part of the organ, benefits from ample anatomical context information. In contrast, the pancreatic head and tail, located at the periphery, suffer from a scarcity of reliable 3D contextual cues. This poses a challenge for our distance regression task, which struggles to maintain precision in these regions due to the presence of blurry boundaries and limited spatial information.

5.4. Limitations and Future Works

Despite the strong performance of DBiSL, several limitations warrant future study. Specifically, our experiments focus on Whole Tumor segmentation on BraTS 2019 to follow the canonical semi-supervised benchmarking protocol and enable fair comparisons with prior work. This evaluation does not cover clinically important multi-class targets (e.g., Tumor Core and Enhancing Tumor). Technically, DBiSL readily generalizes to multi-class segmentation by increasing the output channels of the segmentation/regression heads and applying the task-transformation modules in a channel-wise

manner, while keeping the bidirectional interaction and synergistic losses unchanged. Future work will extend DBiSL to more realistic settings, including multi targets, incomplete annotations and modalities, to improve robustness and clinical utility under heterogeneous data conditions.

6. Conclusion

In this work, we introduced DBiSL, a novel differentiable bidirectional synergistic learning framework for semi-supervised 3D medical image segmentation. It overcomes limitations of unidirectional dual-task methods via a fully differentiable bidirectional transformer, enabling genuine online inter-task bidirectional synergy. Unifying supervised learning, consistency regularization, uncertainty estimation, and pseudo-supervision within a coherent architecture, DBiSL synergistically boosts segmentation performance under severe label scarcity, achieving state-of-the-art results on two benchmarks. Beyond performance, DBiSL provides key insights into unified SSL framework design via dual-task collaboration, establishing a robust bidirectional interaction paradigm for future SSL and broader multi-task vision applications.

Acknowledgements

This work was supported by the National Natural Science Foundation of China under Grant 62401481, Natural Science Foundation of Sichuan Province under Grant 2025ZNSFSC1450, China Postdoctoral Science Foundation under Grant 2024M752683.

References

Adiga, S., Dolz, J., Lombaert, H., 2024. Anatomically-aware uncertainty for semi-supervised image segmentation. *Medical Image Analysis* 91, 103011.

Bai, Y., Chen, D., Li, Q., Shen, W., Wang, Y., 2023. Bidirectional copy-paste for semi-supervised medical image segmentation, in: Proceedings of the IEEE/CVF conference on computer vision and pattern recognition, pp. 11514–11524.

Chen, J., Zhang, J., Debattista, K., Han, J., 2022. Semi-supervised unpaired medical image segmentation through task-affinity consistency. *IEEE Transactions on Medical Imaging* 42, 594–605.

Hamghalam, M., Wang, T., Lei, B., 2020. High tissue contrast image synthesis via multistage attention-gan: application to segmenting brain mr scans. *Neural Networks* 132, 43–52.

Han, K., Liu, L., Song, Y., Liu, Y., Qiu, C., Tang, Y., Teng, Q., Liu, Z., 2022. An effective semi-supervised approach for liver ct image segmentation. *IEEE Journal of Biomedical and Health Informatics* 26, 3999–4007.

Han, K., Sheng, V.S., Song, Y., Liu, Y., Qiu, C., Ma, S., Liu, Z., 2024. Deep semi-supervised learning for medical image segmentation: A review. *Expert Systems with Applications* 245, 123052. URL: <https://www.sciencedirect.com/science/article/pii/S0957417423035546>, doi:<https://doi.org/10.1016/j.eswa.2023.123052>.

Hou, J., Ding, X., Deng, J.D., 2022. Semi-supervised semantic segmentation of vessel images using leaking perturbations, in: Proceedings of the IEEE/CVF winter conference on applications of computer vision, pp. 2625–2634.

Hu, P., Li, X., Tian, Y., Tang, T., Zhou, T., Bai, X., Zhu, S., Liang, T., Li, J., 2020. Automatic pancreas segmentation in ct images with distance-based saliency-aware denseaspp network. *IEEE journal of biomedical and health informatics* 25, 1601–1611.

Isensee, F., Jaeger, P.F., Kohl, S.A., Petersen, J., Maier-Hein, K.H., 2021. nnu-net: a self-configuring method for deep learning-based biomedical image segmentation. *Nature methods* 18, 203–211.

Jiao, R., Zhang, Y., Ding, L., Xue, B., Zhang, J., Cai, R., Jin, C., 2024. Learning with limited annotations: a survey on deep semi-supervised learning for medical image segmentation. *Computers in Biology and Medicine* 169, 107840.

Li, J., Qi, L., Chen, Q., Zhang, Y.D., Qian, X., 2022. A dual meta-learning framework based on idle data for enhancing segmentation of pancreatic cancer. *Medical Image Analysis* 78, 102342.

Li, J., Shi, H., Chen, W., Liu, N., Hwang, K.S., 2023a. Semi-supervised detection model based on adaptive ensemble learning for medical images. *IEEE Transactions on Neural Networks and Learning Systems*.

Li, J., Zhang, Y., Shi, H., Li, M., Li, Q., Qian, X., 2025. A dual-task synergy-driven generalization framework for pancreatic cancer segmentation in ct scans. *IEEE Transactions on Medical Imaging* 44, 3783–3794. doi:[10.1109/TMI.2025.3566376](https://doi.org/10.1109/TMI.2025.3566376).

Li, J., Zhu, H., Chen, T., Qian, X., 2023b. Generalizable pancreas segmentation via a dual self-supervised learning framework. *IEEE Journal of Biomedical and Health Informatics* 27, 4780–4791.

Li, S., Zhang, C., He, X., 2020. Shape-aware semi-supervised 3d semantic segmentation for medical images, in: *Medical Image Computing and Computer Assisted Intervention-MICCAI 2020: 23rd International Conference, Lima, Peru, October 4–8, 2020, Proceedings, Part I* 23, Springer. pp. 552–561.

Liu, Y., Wang, W., Luo, G., Wang, K., Li, S., 2022. A contrastive consistency semi-supervised left atrium segmentation model. *Computerized Medical Imaging and Graphics* 99, 102092.

Luo, X., Chen, J., Song, T., Wang, G., 2021. Semi-supervised medical image segmentation through dual-task consistency, in: Proceedings of the AAAI conference on artificial intelligence, pp. 8801–8809.

Luo, X., Wang, G., Liao, W., Chen, J., Song, T., Chen, Y., Zhang, S., Metaxas, D.N., Zhang, S., 2022. Semi-supervised medical image segmentation via uncertainty rectified pyramid consistency. *Medical Image Analysis* 80, 102517.

Ma, J., Wei, Z., Zhang, Y., Wang, Y., Lv, R., Zhu, C., Gaox-

iang, C., Liu, J., Peng, C., Wang, L., et al., 2020. How distance transform maps boost segmentation cnns: an empirical study, in: Medical Imaging with Deep Learning, PMLR. pp. 479–492.

Malhotra, A., Mittal, S., Majumdar, P., Chhabra, S., Thakral, K., Vatsa, M., Singh, R., Chaudhury, S., Pudrod, A., Agrawal, A., 2022. Multi-task driven explainable diagnosis of covid-19 using chest x-ray images. Pattern recognition 122, 108243.

Menze, B.H., Jakab, A., Bauer, S., Kalpathy-Cramer, J., Farahani, K., Kirby, J., Burren, Y., Porz, N., Slotboom, J., Wiest, R., et al., 2014. The multimodal brain tumor image segmentation benchmark (brats). IEEE transactions on medical imaging 34, 1993–2024.

Miao, J., Chen, C., Liu, F., Wei, H., Heng, P.A., 2023. Caussl: Causality-inspired semi-supervised learning for medical image segmentation, in: Proceedings of the IEEE/CVF International Conference on Computer Vision, pp. 21426–21437.

Milletari, F., Navab, N., Ahmadi, S.A., 2016. V-net: Fully convolutional neural networks for volumetric medical image segmentation, in: 2016 fourth international conference on 3D vision (3DV), IEEE. pp. 565–571.

Ran, L., Li, Y., Liang, G., Zhang, Y., 2024. Pseudo labeling methods for semi-supervised semantic segmentation: A review and future perspectives. IEEE Transactions on Circuits and Systems for Video Technology , 1–1doi:[10.1109/TCSVT.2024.3508768](https://doi.org/10.1109/TCSVT.2024.3508768).

Riba, E., Mishkin, D., Ponsa, D., Rublee, E., Bradski, G., 2020. Kornia: an open source differentiable computer vision library for pytorch, in: Proceedings of the IEEE/CVF Winter Conference on Applications of Computer Vision, pp. 3674–3683.

Roth, H.R., Lu, L., Farag, A., Shin, H.C., Liu, J., Turkbey, E.B., Summers, R.M., 2015. Deeporgan: Multi-level deep convolutional networks for automated pancreas segmentation, in: International conference on medical image computing and computer-assisted intervention, Springer. pp. 556–564.

Shi, Y., Zhang, J., Ling, T., Lu, J., Zheng, Y., Yu, Q., Qi, L., Gao, Y., 2021. Inconsistency-aware uncertainty estimation for semi-supervised medical image segmentation. IEEE transactions on medical imaging 41, 608–620.

Su, J., Luo, Z., Lian, S., Lin, D., Li, S., 2024. Mutual learning with reliable pseudo label for semi-supervised medical image segmentation. Medical Image Analysis 94, 103111.

Tang, H., Zhang, C., Xie, X., 2019. Nodulenet: Decoupled false positive reduction for pulmonary nodule detection and segmentation, in: Medical Image Computing and Computer Assisted Intervention–MICCAI 2019: 22nd International Conference, Shenzhen, China, October 13–17, 2019, Proceedings, Part VI 22, Springer. pp. 266–274.

Tomar, D., Lortkipanidze, M., Vray, G., Bozorgtabar, B., Thiran, J.P., 2021. Self-attentive spatial adaptive normalization for cross-modality domain adaptation. IEEE transactions on medical imaging 40, 2926–2938.

Wang, G., Song, T., Dong, Q., Cui, M., Huang, N., Zhang, S., 2020a. Automatic ischemic stroke lesion segmentation from computed tomography perfusion images by image synthesis and attention-based deep neural networks. Medical Image Analysis 65, 101787.

Wang, H., Qiu, L., Li, Y., Hu, J., Zhang, J., 2024a. Semi-supervised medical image segmentation with strong/weak task-aware consistency, in: Chinese Conference on Pattern Recognition and Computer Vision (PRCV), Springer. pp. 17–31.

Wang, K., Zhan, B., Zu, C., Wu, X., Zhou, J., Zhou, L., Wang, Y., 2022. Semi-supervised medical image segmentation via a tripled-uncertainty guided mean teacher model with contrastive learning. Medical Image Analysis 79, 102447.

Wang, P., Peng, J., Pedersoli, M., Zhou, Y., Zhang, C., Desrosiers, C., 2021. Self-paced and self-consistent co-training for semi-supervised image segmentation. Medical Image Analysis 73, 102146.

Wang, Y., Wei, X., Liu, F., Chen, J., Zhou, Y., Shen, W., Fishman, E.K., Yuille, A.L., 2020b. Deep distance transform for tubular structure segmentation in ct scans, in: Proceedings of the IEEE/CVF Conference on Computer Vision and Pattern Recognition, pp. 3833–3842.

Wang, Y., Xiao, B., Bi, X., Li, W., Gao, X., 2023. Mcf: Mutual correction framework for semi-supervised medical image segmentation, in: Proceedings of the IEEE/CVF conference on computer vision and pattern recognition, pp. 15651–15660.

Wang, Y., Xiao, B., Bi, X., Li, W., Gao, X., 2024b. Boundary-aware prototype in semi-supervised medical image segmentation. IEEE Transactions on Image Processing .

Wang, Y., Zhang, Y., Tian, J., Zhong, C., Shi, Z., Zhang, Y., He, Z., 2020c. Double-uncertainty weighted method for semi-supervised learning, in: Medical Image Computing and Computer Assisted Intervention–MICCAI 2020: 23rd International Conference, Lima, Peru, October 4–8, 2020, Proceedings, Part I 23, Springer. pp. 542–551.

Wu, H., Li, X., Cheng, K.T., 2023. Exploring feature representation learning for semi-supervised medical image segmentation. IEEE Transactions on Neural Networks and Learning Systems .

Wu, J., Wang, Z., Hong, M., Ji, W., Fu, H., Xu, Y., Xu, M., Jin, Y., 2025. Medical sam adapter: Adapting segment anything model for medical image segmentation. Medical Image Analysis 102, 103547. URL: <https://www.sciencedirect.com/science/article/pii/S1361841525000945>, doi:<https://doi.org/10.1016/j.media.2025.103547>.

Xing, Z., Wan, L., Fu, H., Yang, G., Yang, Y., Yu, L., Lei, B., Zhu, L., 2025. Diff-unet: A diffusion embedded network for robust 3d medical image segmentation. Medical Image Analysis , 103654.

Xing, Z., Ye, T., Yang, Y., Cai, D., Gai, B., Wu, X.J., Gao, F., Zhu, L., 2026. Segmamba-v2: Long-range sequential modeling mamba for general 3-d medical image segmentation. IEEE Transactions on Medical Imaging 45, 4–15. doi:[10.1109/TMI.2025.3589797](https://doi.org/10.1109/TMI.2025.3589797).

Xiong, Z., Xia, Q., Hu, Z., Huang, N., Bian, C., Zheng, Y., Vesal, S., Ravikumar, N., Maier, A., Yang, X., Heng, P.A., Ni, D., Li, C., Tong, Q., Si, W., Puybareau, E., Khoudli, Y., Géraud, T., Chen, C., Bai, W., Rueckert, D., Xu, L., Zhuang, X., Luo, X., Jia, S., Serment, M., Liu, Y., Wang, K., Borra, D., Masci, A., Corsi, C., de Vente, C., Veta, M., Karim, R., Preetha, C.J., Engelhardt, S., Qiao, M., Wang, Y., Tao, Q., Nuñez-Garcia, M., Camara, O., Savioli, N., Lamata, P., Zhao, J., 2021. A global benchmark of algorithms for segmenting the left atrium from late gadolinium-enhanced cardiac magnetic resonance imaging. Medical Image Analysis 67, 101832. URL: <https://www.sciencedirect.com/science/article/pii/S1361841520301961>, doi:<https://doi.org/10.1016/j.media.2020.101832>.

Xu, C., Zhang, T., Zhang, D., Zhang, D., Han, J., 2024. Deep generative adversarial reinforcement learning for semi-supervised segmentation of low-contrast and small objects in medical images. *IEEE Transactions on Medical Imaging* 43, 3072–3084. doi:[10.1109/TMI.2024.3383716](https://doi.org/10.1109/TMI.2024.3383716).

Xu, X., Lian, C., Wang, S., Zhu, T., Chen, R.C., Wang, A.Z., Royce, T.J., Yap, P.T., Shen, D., Lian, J., 2021. Asymmetric multi-task attention network for prostate bed segmentation in computed tomography images. *Medical image analysis* 72, 102116.

Xu, Z., Wang, Y., Lu, D., Luo, X., Yan, J., Zheng, Y., Tong, R.K.y., 2023. Ambiguity-selective consistency regularization for mean-teacher semi-supervised medical image segmentation. *Medical Image Analysis* 88, 102880.

Xu, Z., Wang, Y., Lu, D., Yu, L., Yan, J., Luo, J., Ma, K., Zheng, Y., Tong, R.K.y., 2022. All-around real label supervision: Cyclic prototype consistency learning for semi-supervised medical image segmentation. *IEEE Journal of Biomedical and Health Informatics* 26, 3174–3184. doi:[10.1109/JBHI.2022.3162043](https://doi.org/10.1109/JBHI.2022.3162043).

Yang, L., Wang, H., Zeng, Q., Liu, Y., Bian, G., 2021. A hybrid deep segmentation network for fundus vessels via deep-learning framework. *Neurocomputing* 448, 168–178.

Yang, L., Zhao, Z., Zhao, H., 2025. Unimatch v2: Pushing the limit of semi-supervised semantic segmentation. *IEEE Transactions on Pattern Analysis and Machine Intelligence* .

Yu, L., Wang, S., Li, X., Fu, C.W., Heng, P.A., 2019. Uncertainty-aware self-ensembling model for semi-supervised 3d left atrium segmentation, in: *Medical image computing and computer assisted intervention–MICCAI 2019: 22nd international conference, Shenzhen, China, October 13–17, 2019, proceedings, part II* 22, Springer. pp. 605–613.

Zhang, Y., Jiao, R., Liao, Q., Li, D., Zhang, J., 2023. Uncertainty-guided mutual consistency learning for semi-supervised medical image segmentation. *Artificial Intelligence in Medicine* 138, 102476.

Zhao, X., Fang, C., Fan, D.J., Lin, X., Gao, F., Li, G., 2022. Cross-level contrastive learning and consistency constraint for semi-supervised medical image segmentation, in: *2022 IEEE 19th International Symposium on Biomedical Imaging (ISBI)*, IEEE. pp. 1–5.

Zhou, T., Fu, H., Chen, G., Shen, J., Shao, L., 2020a. Hi-net: hybrid-fusion network for multi-modal mr image synthesis. *IEEE transactions on medical imaging* 39, 2772–2781.

Zhou, Y., Wang, B., Huang, L., Cui, S., Shao, L., 2020b. A benchmark for studying diabetic retinopathy: segmentation, grading, and transferability. *IEEE transactions on medical imaging* 40, 818–828.

Zhu, J., Bolsterlee, B., Chow, B.V., Song, Y., Meijering, E., 2024. Hybrid dual mean-teacher network with double-uncertainty guidance for semi-supervised segmentation of magnetic resonance images. *Computerized Medical Imaging and Graphics* 115, 102383. URL: <https://www.sciencedirect.com/science/article/pii/S089561124000600>, doi:<https://doi.org/10.1016/j.compmedimag.2024.102383>.